Science Advances
AAAS

advances.sciencemag.org/cgi/content/full/5/11/eaay0527/DC1

Supplementary Materials for

Electrically driven optical interferometry with spins in silicon carbide

Kevin C. Miao, Alexandre Bourassa, Christopher P. Anderson, Samuel J. Whiteley, Alexander L. Crook, Sam L. Bayliss, Gary Wolfowicz, Gergő Thiering, Péter Udvarhelyi, Viktor Ivády, Hiroshi Abe, Takeshi Ohshima, Ádám Gali, David D. Awschalom*

*Corresponding author. Email: awsch@uchicago.edu

Published 22 November 2019, *Sci. Adv.* **5**, eaay0527 (2019)
DOI: 10.1126/sciadv.aay0527

This PDF file includes:

Section S1. Single-photon emission properties of *kh* VVs
Section S2. Ground- and excited-state spin-spin interactions
Section S3. Spectral diffusion of optical transitions
Section S4. dc Stark tuning of *kh* VVs
Section S5. Integrated multiphoton resonance lineshape
Section S6. Electrical properties of on-chip planar capacitor
Section S7. Ground-state ZEFOZ spin transitions
Section S8. Nuclear spin bath interactions
Section S9. Density functional theory calculations of *kh* VV excited-state structure
Section S10. Density functional theory calculations of electric field–dependent phenomena
Fig. S1. Correlation spectroscopy of a single *kh* VV.
Fig. S2. Spectral diffusion of a single *kh* VV.
Fig. S3. dc Stark shifts of single *kh* VVs.
Fig. S4. Photoluminescence of multiphoton resonances.
Fig. S5. Nonresonant device properties.
Fig. S6. Pulsed optically detected magnetic resonance of single *kh* VVs.
Fig. S7. Cluster-correlation expansion simulations of *kh* VVs.
Table 1. Zero-field splitting values for *kh* VVs.
Table 2. Calculated electric dipole for the ground state–excited state optical transition for the diamond nitrogen-vacancy center and *hh* and *kh* VVs.
References (*34–40*)

Supplemental Materials

Section S1. Single-photon emission properties of *kh* VVs

Single *kh* divacancies (VVs) are expected to follow sub-poissonian photon emission statistics and exhibit antibunching as the optical transition addresses a two-level system. We confirm this by performing correlation spectroscopy on the emission of a single *kh* VV under off-resonant 905 nm excitation. The second order correlation function $g^{(2)}(\tau)$ quantifies the intensity correlations of photon emission events as a function of time τ from another photon emission event. Since a single-photon emitter cannot emit more than one photon at any given moment, we expect the intensity at zero time difference to be zero, $g^{(2)}(0) = 0$.
We detect photons in a Hanbury-Brown-Twiss configuration, where the emission from the defect impinges on the input of a 50/50 beamsplitter and the two outputs are routed to individual channels of a superconducting nanowire single-photon detector. By histogramming the photon arrival time differences between the two detector channels, we find a dip at a time difference $\tau = 0$ reaching $g^{(2)}(0) = 0.269$ without background subtraction, indicating single-photon emission but also non-negligible coincidence counts with background fluorescence (Fig. S1A). We perform a background subtraction procedure (39) using a signal-to-background ratio of 5.77:1 (Fig. S1b), producing a background-subtracted value of $g^{(2)}(0) = 0.005$ (Fig. S1A, inset) and confirming high-fidelity single-photon emission of single *kh* VVs.

Section S2. Ground- and excited-state spin-spin interactions

The spin-1 nature of the ground and excited state spin gives rise to dipolar spin-spin interactions which manifest as longitudinal and transverse zero-field splittings *D* and *E*. *D* and *E* are determined by the ellipsoidicity and rhombicity of the electronic wavefunction distribution, respectively. At $\mathbf{B}_{\text{eff}} \approx \mathbf{0}$, we probe the spin transition frequencies between $|0\rangle$, $|-\rangle$, and $|+\rangle$ and their respective spin-conserving optical transitions in single *kh* VVs to establish values for *D* and *E* in both the ground and excited state. In the ground state, *kh* VVs have a value of *D* similar to that of other VV orientations (3). The basal orientation of the defect and the resulting neighboring lattice configuration leads to a non-axial electronic wavefunction distribution, with a corresponding non-zero *E* in the ground state. In the excited-state, *D* is similar to values obtained for *c*-axis VVs (10), while *E* is significantly larger than its ground-state counterpart. We note that since $|E_{\text{ES}}| > |D_{\text{ES}} / 3|$ in the ground-state basis, a rotation can be made to yield *D*′ and *E*′ so that $|E'_{\text{ES}}| < |D'_{\text{ES}} / 3|$. By rotating the tensor 90° about the *y*-axis, we set our new coordinate system to be $z' = x$, $y' = y$, and $x' = -z$. In this basis

$$D' = \frac{3}{2}\left(E - D/3\right) \tag{S1}$$

$$E' = \frac{1}{2}\left(E + D\right) \tag{S2}$$

which correspond to $D' = -1.203$ GHz and $E' = 237$ MHz (see Table 1). $D' < 0$ in the excited state indicates that the electronic wavefunction distribution is prolate (elongated) along the *z*′-axis. Although this distortion between the ground and excited state electronic wavefunction distribution perturbs the positions of the nearby lattice sites, the spin basis of $\{|0\rangle, |-\rangle, |+\rangle\}$ is invariant under changes of *D* and *E* and the spin Hamiltonian at $\mathbf{B}_{\text{eff}} = \mathbf{0}$ is undisturbed if changes in hyperfine interactions between the ground and excited state are neglected.

Section S3. Spectral diffusion of optical transitions

The presence of impurities other than VVs in the 4H-SiC sample introduces charge trap sites that can either destabilize VV into other charge states, or induce spurious Stark shifts as the trap site varies in charge state. Detailed studies in VV ensembles (34) and single VVs (7) have reported excitation wavelength-dependent photoionization of VVs, converting neutral divacancies to dark charge states. By treating a trap site as a single fluctuating elementary charge at a distance of 100 nm away from the VV, we estimate the magnitude of the induced electric field to be *O*(100 kV/m), which corresponds to *O*(100 MHz) shifts of the excited-state orbital energy for a typical VV. We address this challenge by applying dc electric fields, creating a depletion region in a volume around the VV. This depletion region is marked by a reduction in fluctuating charge carriers, which decreases the absorption rate of the VV with regards to capturing a charge, and also reduces the charge fluctuation rate of nearby trap sites (7).

We quantify the magnitude of this charge fluctuation by repeatedly acquiring photoluminescence excitation (PLE) spectra on a single *kh* VV under an applied dc electric field. We alternate between a 905 nm initialization pulse and a narrow-line laser pulse that is swept across the resonance, all while a dc electric field is applied. At an applied field of 1 MV/m, we produce a depletion region large enough that fast (>1 Hz) charge fluctuations of nearby trap sites are diminished, narrowing the optical transition linewidths to about 20 MHz and allowing us to resolve small fluctuations (<10 MHz) using the narrow optical resonance (Fig. S2A). We take 100 PLE scans, each taking 75 seconds to complete. In each scan we observe charge fluctuations as shifts of the optical resonance's center frequency. By histogramming each scan's center frequency, we find a broad distribution over 100 scans, which suggests that the charge fluctuations are caused by a small ensemble of trap sites (Fig. S2B). The residual fluctuations can be attributed to photoionization effects of the 905 nm initialization laser, as well as the finite size of the depletion region created by the applied electric field.

Section S4. dc Stark tuning of *kh* VVs

In *c*-axis divacancies, dc Stark tuning has been observed using transverse (orthogonal to the defect axis) and longitudinal (parallel to the defect axis) electric fields. The effect of the transverse field is to split the ^{3}E orbital into two separate orbital branches, much like the effect of the transverse crystal field in *kh* divacancies, while a longitudinal field shifts all levels with equal displacement (38). In *kh* divacancies, the large transverse crystal field acts as a large in-built transverse strain, which splits the two orbital branches by order meV. Additional electric fields, either transverse or longitudinal, with magnitudes much smaller than the transverse crystal field serve to linearly perturb the excited-state energy level.

We observe dc Stark shifts by applying a dc electric field across the capacitor. By measuring the resonance frequency of the $|0\rangle \leftrightarrow |A_0'\rangle$ optical transition, we can quantify the *kh* VV's response to dc electric fields (Fig. S3A,B). Initially, at low applied fields, we observe no dc Stark shifts. This observation can be explained by mobile charge carriers spatially rearranging around the *kh* VV under illumination, producing an equal and opposite electric field vector to the applied field. This phenomenon has also been reported in VVs in SiC homojunctions (7), where a characteristic turn-on applied field is required before a complete depletion region is formed and Stark shifts are possible. Starting around 0.4 MV/m, we observe a blueshift of the $|0\rangle \leftrightarrow |A_0'\rangle$ resonance, which continues in a near-linear trend up to 3 MV/m.

We attribute the nonlinear Stark shift behavior near zero applied dc electric field to the creation of a non-uniform depletion region. Only at a critical field does the gap between the capacitor plates become fully depleted, at which point dc Stark shifts are observed. However, we do not expect

this nonlinearity to affect high-frequency ac electric fields, given a characteristic Maxwell relaxation time of mobile charge carriers. When the applied electric field fluctuates on timescales much longer than the Maxwell relaxation time, the mobile charge carriers can respond to the non-equilibrium electric field by spatially rearranging to cancel out the electric field. At shorter fluctuation timescales corresponding to high-frequency ac electric field drives, the mobile charge carriers do not move significantly in one period of the electric field fluctuations, resulting in negligible field cancellation. If mobile charge carriers produced significant screening, a sinusoidal electric field drive would be distorted at low amplitudes and would yield higher-order harmonics in the Landau-Zener-Stückelberg (LZS) spectrum. We qualitatively confirm that this is not the case at GHz frequencies in Fig. 3b of the main text, where the experimental data is well-described by a simulation using a sinusoidal drive and no higher order harmonics are observed at low drive amplitudes.

Section S5. Integrated multiphoton resonance lineshape

The steady-state excited state population expression for the *n*th resonance is

$$A_e(n) \approx \frac{T_1 \Delta_n^2}{2} \tag{S3}$$

where Ω is the optical Rabi frequency, $J_n(x)$ are Bessel functions of the first kind, $\mathcal{A}$ is the amplitude of the induced Stark shift from the ac electric field, ω is the ac electric field frequency, T_1 is the radiative decay time, and T_2 is the optical coherence time. The area of the *n*th resonance is then

$$\begin{aligned} A_e(n) &= \int_{-\infty}^{\infty} P_e\left(\delta'; n\right) d\delta' \\ &= \frac{\pi T_1 \Delta_n^2}{\sqrt{4\pi^2 + T_1 T_2 \Delta_n^2}} \end{aligned} \tag{S4}$$

We show this by summing the photoluminescence within the carrier resonance of the LZS spectrum as a function of applied ac electric field amplitude, $|\mathbf{F}_k|$ (Fig. S4). We expect the intensity $A_e(0)$ to follow a norm-Bessel dependence, $|J_n(x)|$, in the limit of strong driving $T_1 T_2 \Omega_n^2 \gg 4\pi^2$. This can be seen by assessing $A_e(n)$ in that limit

$$A_e(n) \approx \pi \sqrt{\frac{T_1}{T_2}} \left|\Delta_n\right| \tag{S5}$$

In systems where relaxation mechanisms are more intense than the realizable two-level system Rabi frequency, the expected dependence of the integrated time-normalized excited-state population follows a squared-Bessel function, $J_n(x)^2$. Again, this can be confirmed by assessing $A_e(n)$ in the limit $T_1 T_2 \Omega_n^2 \ll 4\pi^2$

$$A_e(n) \approx \frac{T_1 \Delta_n^2}{2} \tag{S6}$$

which qualitatively agrees with the behavior near the Bessel local minima. This strong dependence on coherence time has been used in prior works to characterize the intensity of the relaxation mechanisms of a two-level system (35,37).
Optical linewidths in the zero dc bias regime can reach 440 MHz under strong optical drive, as shown in Fig. S4b. This confirms that the strong driving regime is achieved and the condition to observe norm-Bessel photoluminescence as a function of applied ac electric field amplitude is satisfied.

Section S6. Electrical properties of on-chip planar capacitor

The planar capacitor structure on the sample is comprised of two parallel planar plates of Ti/Au, each of width 10 μm and length 100 μm, with a gap width of 10 μm. Considering the SiC substrate with a relative permittivity of $\varepsilon_0 = 9.66$, we obtain a capacitance of 7.7 fF for the capacitor structure. In this geometry, we produce a high-pass filter, where the GHz-frequency range used in our experiments are reflected and yield maximal electric field across the gap. We characterize the behavior of the capacitor by measuring the input voltage port reflection coefficient S_{11} (Fig. S5A). At low frequencies, we find the structure to be mostly reflective, with decreasing reflectivity at higher frequencies, characteristic of a high-pass filter. While the reflectivity exhibits oscillations characteristic of cable resonances, we do not find a strong resonance in the GHz-frequency range. Losses through the cable do not exceed −3.5 dB throughout the probe frequency range and are neglected.
The non-resonant structure allows for broadband tuning of the drive frequency. We demonstrate this by observing LZS interference fringes as a function of ac electric drive frequency (Fig. S5B). With a fixed ac electric field drive amplitude, we vary the frequency of the drive and obtain photoluminescence excitation spectra. We find broad fluctuations in fluorescence as the quantity $x = \mathcal{A} / \omega$ changes, as well as more rapid fluctuations from cable resonances. However, no obvious resonances arising from the capacitor are found. Qualitatively, this confirms that our electric field interaction is not enhanced by any resonant behavior of the capacitor, and that further enhancements can be attained with an intentionally resonant structure.

Section S7. Ground-state ZEFOZ spin transitions

At $\mathbf{B}_{\text{eff}} = \mathbf{0}$, the effect of E_{GS} is to mix the $S_z = \{|-1\rangle, |0\rangle, |+1\rangle\}$ eigenbasis into $|0\rangle$, $|+\rangle = \frac{1}{\sqrt{2}}\left(|+1\rangle + |-1\rangle\right)$, and $|-\rangle = \frac{1}{\sqrt{2}}\left(|+1\rangle - |-1\rangle\right)$. An eigenbasis containing $|+\rangle$ and $|-\rangle$ allows for magnetic driving of the $|+\rangle \leftrightarrow |-\rangle$ transition by virtue of $\langle +|S_z|-\rangle \neq 0$. Knowing this, we can apply magnetically-driven spin rotations to reach all spin eigenstates in combination with at least one of the spin rotations enabled by $\langle 0|S_x|+\rangle \neq 0$ or $\langle 0|S_y|-\rangle \neq 0$. We demonstrate the ability to span the eigenbasis by performing optically-detected magnetic resonance (ODMR) on both the $|0\rangle \leftrightarrow |+\rangle$ and $|+\rangle \leftrightarrow |-\rangle$ transitions. We find these resonances at $D_{\text{GS}} + E_{\text{GS}} = 1.352373$ GHz and $2E_{\text{GS}} = 36.839$ MHz, respectively (Fig. S6). While the $|0\rangle \leftrightarrow |-\rangle$ transition can also be driven, the magnetic dipole of that transition is not well aligned with the magnetic driving field in our experiments. Consequently, the large drive power necessary to perform spin driving of the $|0\rangle \leftrightarrow |-\rangle$ transition produces significant off-resonant driving of the well-coupled $|0\rangle \leftrightarrow |+\rangle$ transition, which obscures ODMR contrast and suppresses spin-rotation fidelity. This limitation can be overcome by introducing a more extreme miscut on the substrate to tilt the magnetic dipole out of plane, or by fabricating transparent drive wires above the defect to produce an in-plane drive field.

Section S8. Nuclear spin bath interactions

Naturally abundant silicon carbide consists of non-zero nuclear spin isotopes of Si and C. Specifically, Si is comprised of 4.69% ^{29}Si and C is comprised of 1.07% ^{13}C, both of which are spin-½. As these nuclear spins undergo dipolar interactions with each other, the magnetic field environment of the VV fluctuates, resulting in inhomogeneous broadening of VV spin resonances. This broadening most readily manifests in the finite spin dephasing times that we observe when the spin is prepared into a superposition state.

By virtue of operating at a ZEFOZ point, the *kh* VV spin is resilient to magnetic field fluctuations, which results in significantly lengthened spin dephasing times compared to *c*-axis VVs. However, residual fluctuations in the spin resonance frequency still occur given the non-zero higher-order derivatives of the energy dispersion. We use Cluster Correlation Expansion (CCE) simulations to quantify these fluctuations (2) and arrive upon estimates for T_2^* for *kh* VVs prepared into $|\psi_0\rangle = \frac{1}{\sqrt{2}}(|0\rangle + |+\rangle)$ at low external magnetic field.

We sample 20 randomly-generated nuclear spin configurations and average the dynamics predicted by CCE2 (second-order CCE) for various fields between 0.01 G and 1 G (Fig. S7A). We find that as the external magnetic field approaches 0 G, the spin dephasing time of the superposition $|\psi_0\rangle$ increases (Fig. S7B). However, we note that our simulations predict a singularity for T_2^* at $B_z = 0$, which arises from the vanishing derivative of the energy dispersion at $\mathbf{B}_{\text{eff}} = \mathbf{0}$ combined with the fact our CCE model ignores nuclear spin-induced backaction on the VV electron spin. To address this, we incorporate the effects of an Overhauser field, which manifests as classical, Gaussian-distributed fluctuations of the magnetic field (40). The magnitude of the Overhauser field can be estimated from *c*-axis VV spin dephasing times at high field, where the limiting factor for T_2^* is macroscopic magnetic field fluctuations, $\Delta B = \frac{\Delta \nu}{g \mu_B} = \frac{1}{g \mu_B \pi T_2^*}$. We then model the low-field behavior of *kh* VVs by convolving the spin response obtained through CCE2 simulations over a Gaussian distribution of magnetic fields, the width of which is determined by ΔB. We use a *c*-axis VV high-field T_2^* value of 1 μs, which corresponds to $\Delta B \approx$ 0.1 G. With decreasing B_z, we find that at $B_z \approx \Delta B$ the spin dephasing time begins saturating towards 105 μs. This agrees with the experimental value of 74 μs after considering imperfect field cancellation on the order of 0.1 G, as well as variations of nuclear spin configurations leading to variations in characteristic T_2^* times.

Section S9. Density functional theory calculations of *kh* VV excited-state structure

By considering a C_{1h} symmetry basal VV configuration as a distorted C_{3v} symmetry *c*-axis oriented VV configuration, we can obtain the excited state structure of the *kh* VV as a perturbation of *c*-axis VV structure. The theory of the ^3E excited state is well established for the C_{3v} symmetry diamond NV-center and *c*-axis VVs (38). At zero strain, the ^3E excited state includes six substates, $|A_1\rangle$, $|A_2\rangle$, $|E_1\rangle$, $|E_2\rangle$, $|E_x\rangle$, and $|E_y\rangle$, whose relative positions are determined by spin-spin interactions, spin-orbit interactions, and the dynamic Jahn-Teller effect (36). In the case of *kh* VVs, the dominant effect is a crystal field splitting which separates the six ^3E states into two branches, each with three substates. The branches correspond to the $|X\rangle = |a_1 e_x - e_x a_1\rangle$ or $|Y\rangle = |a_1 e_y - e_y a_1\rangle$ orbital wavefunctions. In terms of ^3E states, the states in the A'' branch can be expressed as

$$
\begin{aligned}
|A''_{+}\rangle &\approx i\left(|E_2\rangle + |A_2\rangle\right) = |Y\rangle \otimes |+\rangle \\
|A''_{-}\rangle &\approx i\left(|A_1\rangle - |E_1\rangle\right) = |Y\rangle \otimes |-\rangle \\
|A''_{0}\rangle &\approx |E_y\rangle = |Y\rangle \otimes |0\rangle
\end{aligned}
\tag{S7}
$$

and the states in the A' branch as

$$
\begin{aligned}
|A'_{+}\rangle &\approx |E_1\rangle + |A_1\rangle = |X\rangle \otimes |+\rangle \\
|A'_{-}\rangle &\approx |A_2\rangle - |E_2\rangle = |X\rangle \otimes |-\rangle \\
|A'_{0}\rangle &\approx |E_x\rangle = |X\rangle \otimes |0\rangle
\end{aligned}
\tag{S8}
$$

Ab initio calculations (using the PBE functional) show that the splitting between the branches is 3.5 meV and the A' branch is lower in energy. We note that the upper A'' branch corresponds to a metastable atomic configuration as there exists a relaxation path with no barrier from A'' to A'. The spin-orbit interaction, which is the dominant interaction in the C_{3v} symmetry ^3E fine structure, is suppressed by the crystal field in *kh* VVs. Consequently, there is no observable first-order spin-orbit interaction in both branches.

Section S10. Density functional theory calculations of electric field–dependent phenomena

In the ground state of the C_{3v}-symmetric NV-center in diamond and *c*-axis VVs in SiC, it has been established that the spatial part of the $^3A_2$ ground state is stable against strain and electric field variations (38). Due to mixing of the a'_{a1} and a'_e single electron states in C_{1h}-symmetric basal VV configurations, this statement is slightly relaxed. Experimental measurements show, however, that the electric field coupling constant of the spin sublevels remains on the order of 3×10^{-4} GHz/(MV/m) (12), which is negligible compared to the 19 GHz/(MV/m) Stark shift of the GS-ES optical transition energy for basally-oriented VVs obtained in our *ab initio* simulations, which are detailed later. Therefore, we only focus on the Stark effect and excited-state electric field couplings.

The Stark shift is related to the dipole moment of the transition as

$$
H_{\text{el}} = -\mathbf{F} \cdot \mathbf{d}_{\text{GE}} \tag{S9}
$$

where $\mathbf{F}$ is the displacement field and $\mathbf{d}_{\text{GE}}$ is the difference of the point defect's dipole moment between the excited state and the ground state. In order to understand the robustness of the *kh* VV's optical transition, we first discuss C_{3v}-symmetric configurations. In perfect C_{3v} symmetry, the dipole is aligned along the axis of the defect and thus Eq. (S9) simplifies to $H_{\text{el}} = F_z d_z = F_{\parallel} d_{\parallel}$, which linearly shifts the ^3E optical transition energy. This behavior can be attributed to the mutual cancellation of perpendicular components. Indeed, the $|X\rangle = |a_1 e_x - e_x a_1\rangle$ and $|Y\rangle = |a_1 e_y - e_y a_1\rangle$ orbital states have non-zero perpendicular dipole components in a way so that $d_{\perp}^{X} = -d_{\perp}^{Y}$. The perpendicular dipole moment components of $|X\rangle$ and $|Y\rangle$ cancel out either due to the degeneracy of the zero-strain states or due to the mixed spatial states that evenly contain $|X\rangle$ and $|Y\rangle$.

In realistic conditions, perfect C_{3v}-symmetric configurations relax due to the presence of local strain and electric fields. For example, a perturbing perpendicular electric field or anisotropic strain can split the ^3E excited state based on the $|X\rangle$ and $|Y\rangle$ character of the states. As a result, two branches can form, each having either predominantly $|X\rangle$ or $|Y\rangle$ spatial character. At finite temperature, $k_B T$ is expectedly larger than the branch splitting caused by local fields, and thus

spin conserving transitions, mediated by low energy acoustic phonon modes, can thermalize the occupation of the branches. Note that thermal fluctuations of the branch occupation give rise to a time-dependent, randomly fluctuating perpendicular dipole moment component, due to the different dipole moments of the branches. In the presence of a perpendicular electric field, the energy of the thermalized ^3E state will fluctuate and may intensify optical dephasing processes. In *ab ovo* C_{1h} configurations, like the *kh* VV, the perpendicular dipolar coupling components must be distinguished as an in-plane component d_x and an out-of-plane component d_y, where the plane is spanned by the defect axis and the *c*-axis. Due to symmetry reasons, the d_y dipole component must be zero, thus *kh* VVs are insensitive to F_y displacement fields to first order. Furthermore, higher order effects due to F_y that would mix the A' and A'' branches are suppressed by the large crystal field splitting between the branches. Therefore, *kh* VVs are decoupled from F_y and only experience F_x and F_z components of the displacement field.

The dipole moment that corresponds to the GS-ES optical transition can be determined from *ab initio* simulations. The calculated dipole moments for the diamond NV-center, *hh* VV, and *kh* VV can be found in Table 2. Note that in all three configurations (corresponding to a $|X\rangle$ spatial excited state configuration), the parallel component is still the dominant contribution to the electric dipole moment of the defects. As the *kh* VV axis is inclined at an angle of 19.5° with respect to the basal plane, we expect that *kh* VVs can couple to in-plane electric fields about 11 times stronger when compared to *c*-axis VV coupling to in-plane electric fields.

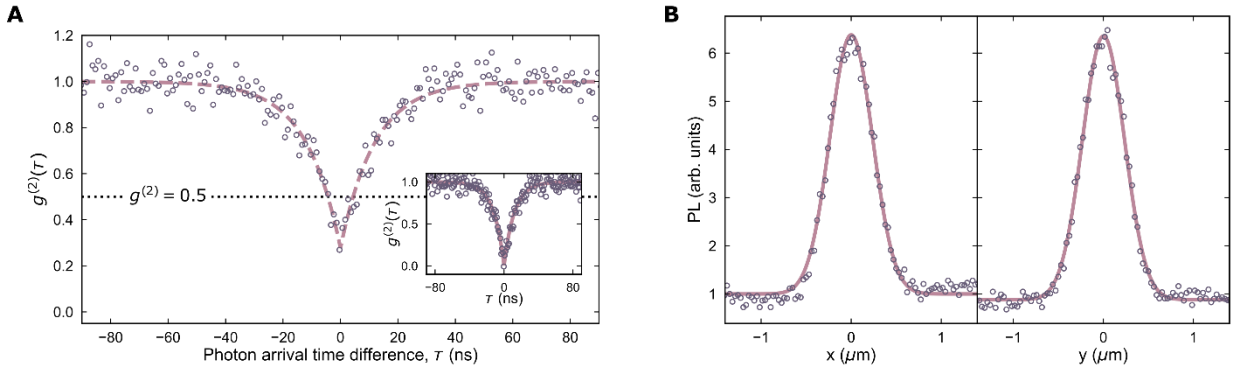

Fig. S1. Correlation spectroscopy of a single *kh* VV. (**A**) Second order correlation function $g^{(2)}$ as a function of photon arrival time difference τ. The dotted line is a best fit to a two-level system model with no background subtraction. $g^{(2)}(0) < 0.5$ indicates single-photon emission. Inset: $g^{(2)}(\tau)$ after background subtraction. (**B**) Photoluminescence line cuts along the *x*- and *y*-axis used to determine signal-to-background ratio used for background subtraction.

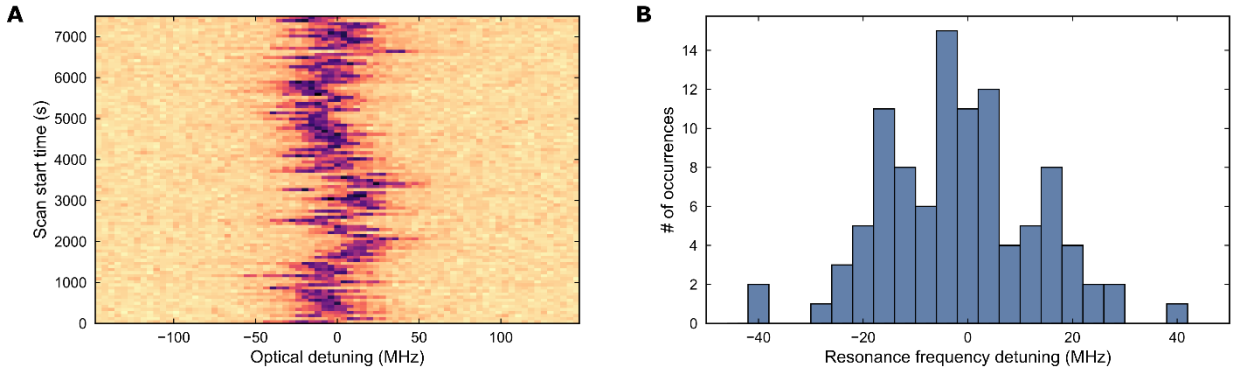

Fig. S2. Spectral diffusion of a single *kh* VV. (**A**) Wandering of the optical resonance central frequency observed in photoluminescence excitation spectra. (**B**) The distribution of optical resonance central frequencies over the course of 100 scans.

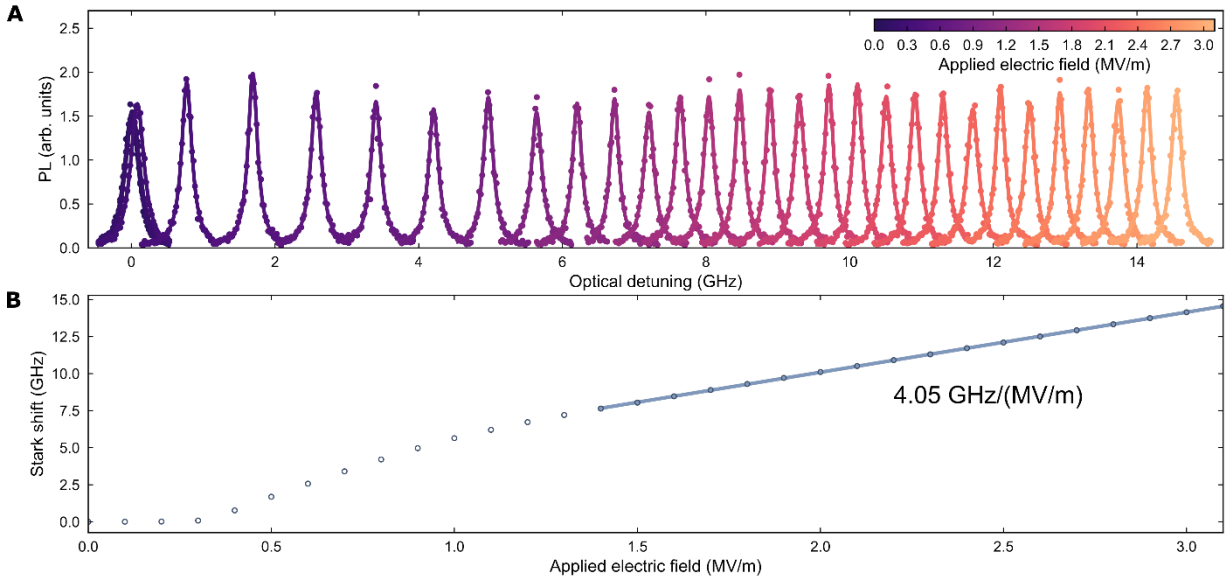

Fig. S3. dc Stark shifts of single *kh* VVs. (**A**) Optical resonance $|0\rangle \leftrightarrow |A_0'\rangle$ at various applied voltages from 0 V to 31 V. (**B**) Center frequencies of the optical resonances in a) as a function of applied voltage. In the linear regime, a Stark shift sensitivity of 4.05 GHz/(MV/m) is observed.

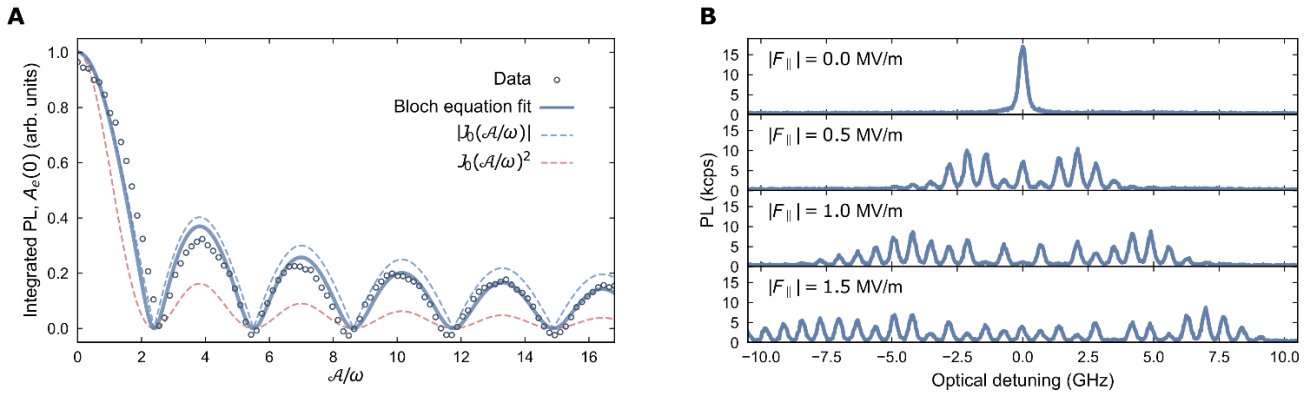

Fig. S4. Photoluminescence of multiphoton resonances. (A) Integrated photoluminescence of carrier resonance. Data (open circles) are best fit to a Bloch equation model with weak relaxation compared to optical driving. Dashed lines indicate expected integrated resonance lineshapes in the limit of vanishing relaxation (blue) and vanishing optical drive (red). **(B)** Line cuts of multiphoton resonances at select electric field amplitudes.

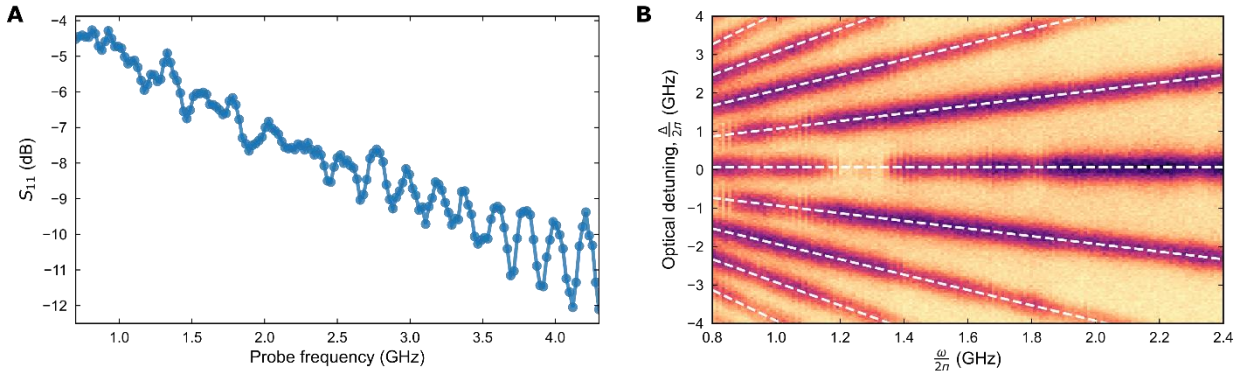

Fig. S5. Nonresonant device properties. (A) S_{11} of device showing capacitive behavior at low frequencies. **(B)** Landau-Zener-Stückelberg interference of a single *kh* VV as a function of electric field modulation frequency. Dashed lines serve as guides to multiphoton resonances, $\Delta = m\omega$, $m = -4,...,4$.

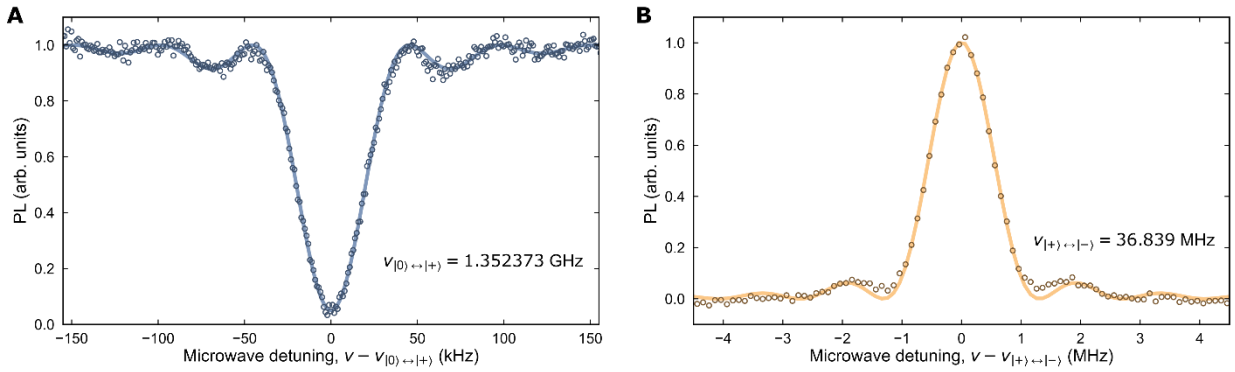

Fig. S6. Pulsed optically detected magnetic resonance of single kh VVs. (**A**) Spin resonance $|0\rangle \leftrightarrow |+\rangle$ located at $D_{GS} + E_{GS}$ = 1.352373 GHz. Photoluminescence acquired from $|0\rangle \leftrightarrow |A_0'\rangle$ transition. (**B**) Spin resonance $|+\rangle \leftrightarrow |-\rangle$ located at $2E_{GS}$ = 36.839 MHz. Photoluminescence acquired from $|-\rangle \leftrightarrow |A_-'\rangle$ transition. Fits are made to a Bloch equation model of a dissipationless two-level system.

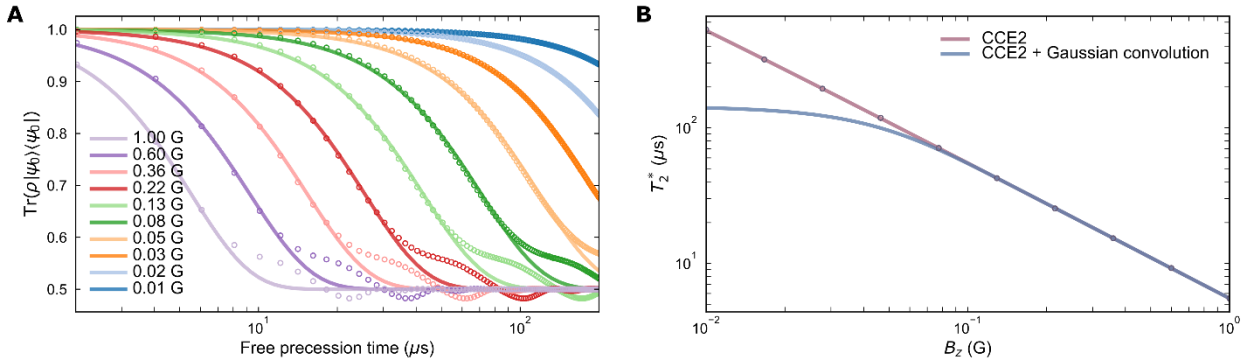

Fig. S7. Cluster-correlation expansion simulations of *kh* VVs. (**A**) CCE2 simulations of spin dynamics when the spin is prepared into $|\psi_0\rangle = \frac{1}{\sqrt{2}}(|0\rangle + |+\rangle)$ at various *z*-oriented magnetic fields. (**B**) T_2^* spin dephasing times derived from the stretched exponential fits of each trace in (**A**). A Gaussian convolution is incorporated into the model to address the singularity at B_z = 0.

Table 1. Zero-field splitting values for *kh* VVs. D and E are the longitudinal and transverse zero-field splitting components, respectively. Values for D and E in the excited state are determined in the same basis as the ground state, as well as after proper diagonalization.

	D (MHz)	*E* (MHz)
GS	1333.95	18.42
ES (GS basis)	957	-483
ES (diagonalized)	-1203	237

Table 2. Calculated electric dipole for the ground state–excited state optical transition for the diamond nitrogen-vacancy center and *hh* and *kh* VVs. Parallel (perpendicular) indicates parallel (perpendicular) to the defect axis and *x* is perpendicular to the defect axis and coplanar with the defect axis and the *c*-axis.

Defect	$d_{\perp}$ (d_x) (GHz/(MV/m))	$d_{\parallel}$ (GHz/(MV/m))
Diamond NV-center (C_{1h} ES, static Jahn-Teller)	1.79	20.43
hh VV (C_{1h} ES, static Jahn-Teller)	1.61	19.07
kh VV (*ab ovo* C_{1h})	0.23	19.17